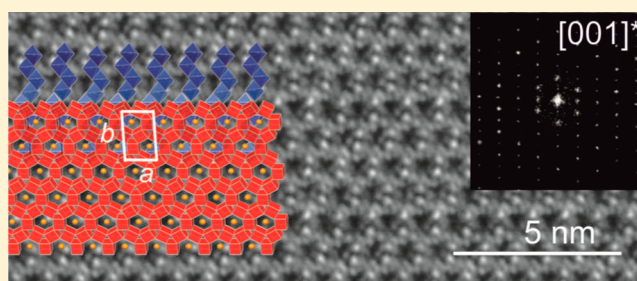


Crystal Growth and Real Structure Effects of the First Weak 3D Stacked Topological Insulator $\text{Bi}_{14}\text{Rh}_3\text{I}_9$ Bertold Rasche,[†] Anna Isaeva,[†] Alexander Gerisch,^{†,||} Martin Kaiser,[†] Wouter Van den Broek,[‡] Christoph T. Koch,[‡] Ute Kaiser,[‡] and Michael Ruck^{*,†,§}[†]Technische Universität Dresden, Helmholtzstr. 10, 01069 Dresden, Germany[‡]University of Ulm, Albert-Einstein-Allee 11, 89081 Ulm, Germany[§]Max Planck Institute for Chemical Physics of Solids, Nöthnitzer Str. 40, 01187 Dresden, Germany

S Supporting Information

ABSTRACT: A detailed account of the crystal-growth technique and real structure effects of the first 3D weak topological insulator $\text{Bi}_{14}\text{Rh}_3\text{I}_9 = [(\text{Bi}_4\text{Rh})_3\text{I}][\text{BiI}_4]_2$ is given. As recently shown, this compound features decorated-honeycomb $[(\text{Bi}_4\text{Rh})_3\text{I}]^{2+}$ sheets with topologically protected electronic edge-states and thereby constitutes a new topological class. Meticulous optimization of the synthesis protocol, using thermochemical methods, yielded high-quality crystals of $\text{Bi}_{14}\text{Rh}_3\text{I}_9$ suitable for the experimental characterization of the structural as well as topological properties. Insightful information about the crystal structure, its pseudosymmetry, and the thereby caused stacking disorder and twinning phenomena, obtained by X-ray diffraction and TEM studies, is crucial for an adequate theoretical modeling of coupling between the topologically nontrivial sheets. As demonstrated here, $\text{Bi}_{14}\text{Rh}_3\text{I}_9$ is not an exotic anomaly, but a stable, structurally well-defined bulk material, which can be used for gaining experimental knowledge about the yet poorly investigated class of weak 3D topological insulators. It could equally foster the synthesis and understanding of related compounds with the bismuth-based decorated-honeycomb sheets.

KEYWORDS: topological insulator, bismuth, $\text{Bi}_{14}\text{Rh}_3\text{I}_9$, crystal growth, twinning, antiphase boundaries, pseudosymmetry



■ INTRODUCTION

Convergence between sophisticated theoretical models and advances in materials science and nanostructurization has recently been achieved in the emergent field of topological insulators (TIs).^{1–9} Owing to the topological protection of surface spin currents by time-reversal and/or bulk symmetries, topological insulators hold fascinating prospects for breakthrough innovations in spintronics.^{10–12} First theoretically predicted, then experimentally observed in Bi_2Te_3 (a so-called strong 3D TI) and HgTe/CdTe quantum wells (2D TI), the topological insulator is a novel state of matter characterized by an insulating bulk but conducting surfaces or edges. The latter features non-dissipative spin currents resilient to backscattering on nonmagnetic impurities at normal conditions. This intriguing property may enable information to be transmitted without incurring any losses, thus paving the way toward fault-tolerant quantum computing.^{13–18}

Despite enormous interest, only a few compounds have hitherto been thoroughly investigated; therefore, the demand for new candidate compounds and, more importantly, for general guidelines on how to obtain a TI is high. Moreover, large high-quality crystals are required for physical property measurements that are performed primarily on the surface. Since topological protection manifests itself in the thin surficial

sample area, it is crucial to study the real structure and defects close to the surface.

Kane and Mele¹⁹ predicted a single graphene sheet to be a topological insulator thanks to the spin-momentum locking and emphasized the deciding role of spin–orbit coupling (SOC) in formation of the topologically protected edge states in a 2D TI. Unfortunately, the SOC effect, opening the topological gap in graphene, is extremely weak and thus of no practical use.^{20,21} With this in mind, hexagonal arrangements of nonradioactive elements with reasonable SOC, namely, ranging from iridium to bismuth, call for a closer look.

The electron-rich element bismuth is particularly promising because it predictably contributes to the electronic states at the Fermi level of its compounds, e.g., bismuth-rich subhalogenides. In these thermodynamically stable materials, a high bismuth content concurs with a great diversity of structural motifs.^{22–24} Among them are planar-hexagonal, graphene-like arrangements that could, in our view, be promising candidates for TIs.²⁵ Very recently the first example of a new topological family, the bismuth-rich subiodide $\text{Bi}_{14}\text{Rh}_3\text{I}_9$, was reported.²⁶

Received: April 3, 2013

Revised: May 17, 2013

Published: May 21, 2013



This layered compound features bismuth-based decorated-honeycomb motifs, each of them being a 2D TI according to the Kane–Mele model. Nonconducting spacer layers in the structure ensure that the interaction between the 2D TI layers is almost vanishing, rendering the material a so-called “weak” 3D topological insulator.

The general theory and especially experimental activities have so far been quite moderate for weak 3D TIs. Experimental proof of the existence of edge states represents a great challenge. We hope that $\text{Bi}_{14}\text{Rh}_3\text{I}_9$ and further members of this class may provide a playground for such studies. Aiming at this, we report on the optimization of the conditions for the crystal growth of $\text{Bi}_{14}\text{Rh}_3\text{I}_9$ and several real structure phenomena connected with the layered structure of the compound.

RESULTS AND DISCUSSION

Thermal Stability and Crystal Growth Optimization.

After the serendipitous discovery of $\text{Bi}_{14}\text{Rh}_3\text{I}_9$ and the recognition of its TI properties,²⁶ great effort has been devoted to the rationalization of the synthesis and the optimization of the crystal growth. The combination of DSC and TG experiments and complementary tempering experiments at derived temperatures allowed us to gain insight into the complex phase relations in the ternary Bi–Rh–I system.

The temperature stability range of $\text{Bi}_{14}\text{Rh}_3\text{I}_9$ has been experimentally evaluated in a closed system under equilibrium conditions as well as in an open system under standard conditions:

At first, it was been established that in a closed system, e.g., a sealed silica ampule, $\text{Bi}_{14}\text{Rh}_3\text{I}_9$ decomposes peritectically at 441 °C (signal A in Figure 1) into a new ternary phase X^{27} plus

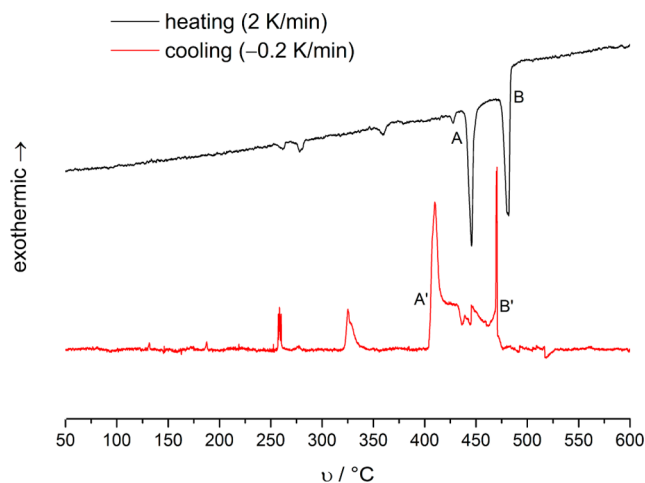


Figure 1. DSC experiment: Heating of $\text{Bi}_{14}\text{Rh}_3\text{I}_9$ and subsequent cooling of the formed melt in a closed system. A: first decomposition step. B: second decomposition step. A': crystallization of $\text{Bi}_{14}\text{Rh}_3\text{I}_9$. B': crystallization of the phase X. Additional peaks on the cooling curve correspond to crystallization of $\text{Bi}_{43}\text{Rh}_3\text{I}_{36}$ (≈ 330 °C) and Bi (≈ 269 °C).

$\text{BiI}_{3(\text{l,g})}$ and $\text{Bi}_{(\text{l})}$. Consequently, the PXRD pattern of a sample that had been tempered at 458 °C and subsequently quenched shows no reflections of $\text{Bi}_{14}\text{Rh}_3\text{I}_9$ but predominantly the phase X and crystalline BiI_3 and BiOI (presumably from BiI_3 hydrolysis in air) (Supporting Information Figure S2). The phase X then decomposes at 475 °C (signal B in Figure 1) into

$\text{BiI}_{3(\text{l,g})}$, the high-temperature modification of $\text{Bi}_2\text{Rh}_{(\text{s})}$ ²⁸ and $\text{Bi}_{(\text{l})}$, as can be expected from the binary phase diagrams.²⁹

Second, it was found that in an open system, e.g., an open alumina crucible under a flow of argon ($p = 1$ bar), $\text{Bi}_{14}\text{Rh}_3\text{I}_9$ decomposes already at 380 °C, as seen from the thermogravimetry (TG) experiment (Figure 2). The differential TG (DTG)

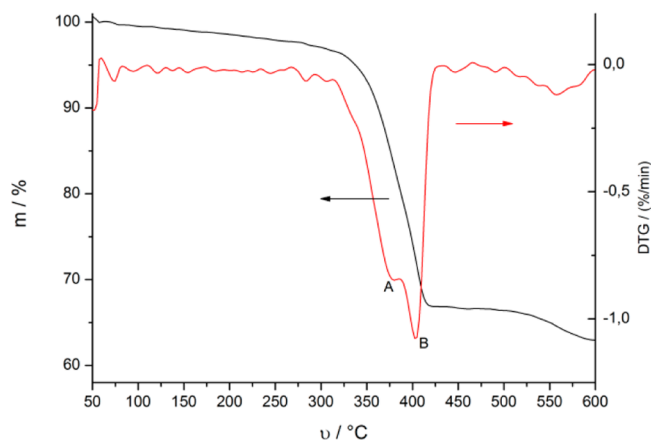


Figure 2. Mass loss and differentiated mass loss of $\text{Bi}_{14}\text{Rh}_3\text{I}_9$ upon heating in a stream of argon (open system: $p = 1$ bar). A: first decomposition step. B: second decomposition step.

curve shows that the two-step decomposition process is similar to the one in the closed system. On the first step at 380 °C, a mixture of $\text{BiI}_{3(\text{l,g})}$, $\text{Bi}_{(\text{l})}$, and the phase X is formed (peak A in Figure 2). The latter compound decomposes on the second step at 400 °C into $\text{BiI}_{3(\text{s,g})}$, $\text{Bi}_4\text{Rh}_{(\text{s})}$, and $\text{Bi}_3\text{Rh}_{(\text{s})}$ (peak B) in accordance with the binary phase diagram.²⁹ At these temperatures the vapor pressure of BiI_3 is in between 0.04 and 0.08 bar, which leads to the observed mass loss in the TG experiment.

The formation of $\text{Bi}_{14}\text{Rh}_3\text{I}_9$ has been studied in a DSC experiment by heating a stoichiometric mixture of Bi, Rh, and BiI_3 (molar ratio 11:3:3) in a closed system and has been attributed to the exothermic signal at 355 °C (see green region in Figure 3). This conclusion is supported by the following findings: Samples tempered at 300 or 330 °C for 1 h (Supporting Information Figures S4 and S5) contained a

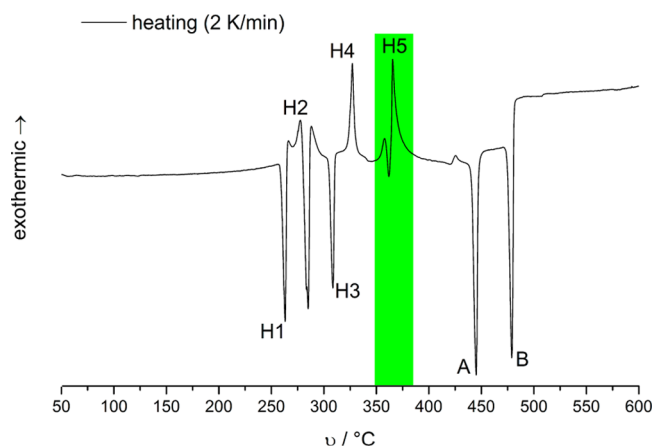


Figure 3. DSC experiment: Heating of a stoichiometric mixture Bi, Rh, and BiI_3 (11:3:3) in a closed system. Highlighted region: formation of $\text{Bi}_{14}\text{Rh}_3\text{I}_9$. Signals are assigned in Table 1.

mixture of $\text{Bi}_9\text{Rh}_2\text{I}_3$,³⁰ $\text{Bi}_4\text{Rh}_3\text{I}_{36}$,³¹ $\text{Bi}_{14}\text{Rh}_3\text{I}_9$, and binary compounds (see Table 1). Samples tempered at 370 °C for 1

Table 1. DSC Signals on Heating of a Mixture of Bi, Rh, and BiI_3 (11:3:3) from Room Temperature to 700 °C

signal	T_{onset} °C	effect	assigned reaction
H1	260	endo- and exothermic	melting of Bi and formation of Bi_4Rh
H2	269	exo- and endothermic	formation of BiI and rt- Bi_2Rh and unknown effect
H3	305	endothermic	decomposition of BiI
H4	324	exothermic	formation of $\text{Bi}_4\text{Rh}_3\text{I}_{36}$
H5	355	exothermic	formation of $\text{Bi}_{14}\text{Rh}_3\text{I}_9$
A	441	endothermic	decomposition of $\text{Bi}_{14}\text{Rh}_3\text{I}_9$
B	475	endothermic	decomposition of phase X

h contained almost exclusively $\text{Bi}_{14}\text{Rh}_3\text{I}_9$ (Supporting Information Figure S1) and minor admixtures of elemental bismuth. Differences between the product spectra of dynamic DSC measurements ($\Delta T/\Delta t = 2$ K/min) and isothermal tempering experiments (1 h) could be rationalized by varying reaction kinetics.

In order to find the optimal crystal-growth parameters, several DSC experiments in a closed system (silica ampule) were performed starting from a homogeneous melt at 600 °C with different cooling rates (from -0.2 K/min up to -10 K/min). Recrystallization of $\text{Bi}_{14}\text{Rh}_3\text{I}_9$ at 410 °C was observed only for the slowest cooling rate of $\Delta T/\Delta t = -0.2$ K/min (signal A' in Figure 1), enabling us to conclude that crystallization from the melt is strongly hindered by kinetics. An independent experiment, in which a melt was cooled from 600 to 365 °C at -0.1 K/min and subsequently quenched (Figure S3 of the Supporting Information), also confirmed that $\text{Bi}_{14}\text{Rh}_3\text{I}_9$ crystallizes on slow cooling.

The recrystallization of the aforementioned phase X was observed at 468 °C at any cooling rate (signal B' in Figure 1). The remaining signals could be attributed to the (pseudo)-binary Bi–Rh and Bi–I systems.²⁹

The optimized synthetic technique, based on the given data, is detailed in the Experimental Section.

Crystal Structure and Defects. $\text{Bi}_{14}\text{Rh}_3\text{I}_9$ has a layered structure that is composed of two alternating types of layers (Figure 4). The marked anisotropy is reflected by the platelet morphology of single crystals (Supporting Information Figure S7). The so-called intermetallic layer is a kagomé-type network of rhodium-centered bismuth cubes that share common edges. Each of the hexagonal prismatic voids in the ${}^2_{\infty}[\text{RhBi}_{8/2}]^+$ net

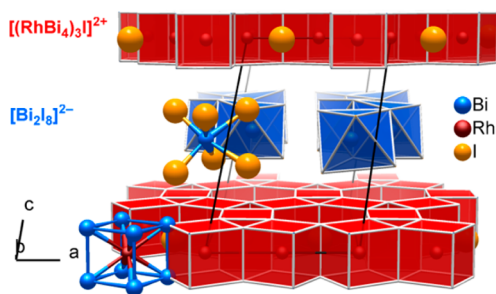


Figure 4. Layered structure of $\text{Bi}_{14}\text{Rh}_3\text{I}_9$, where intermetallic layers (cubes) and layers of iodido-bismuthate chains (octahedra) are alternately stacked.

hosts an iodide ion. The overall composition of the intermetallic layer is the ${}^2_{\infty}[(\text{RhBi}_4)_3\text{I}]^{2+}$. The iodido-bismuthate(III) layer consists of $[\text{Bi}_2\text{I}_{4/2}]^-$ octahedra that share edges to form zigzag chains ${}^1_{\infty}[\text{BiI}_4]^-$, which run along the b -axis. Since the basic features of the structure have already been discussed,²⁶ we will focus on the pseudosymmetries of the two layer types, which give rise to several real-structure effects in the $\text{Bi}_{14}\text{Rh}_3\text{I}_9$ crystals.

Although the overall symmetry of $\text{Bi}_{14}\text{Rh}_3\text{I}_9$ is triclinic (space group $P1$, $a = 916.61(3)$ pm, $b = 1583.61(5)$ pm, $c = 1429.78(5)$ pm, $\alpha = 62.746(1)^\circ$, $\beta = 80.922(2)^\circ$, $\gamma = 89.936(2)^\circ$),³² the intermetallic layer adopts the hexagonal layer group symmetry $p6/mmm$ (Figure 5). The ratio $b/a =$

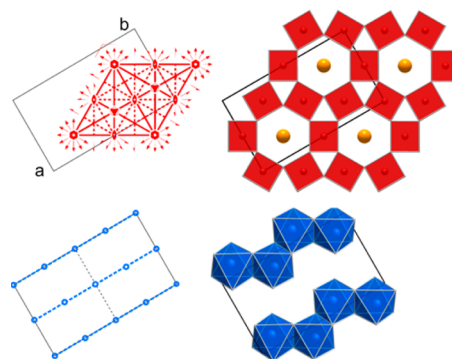


Figure 5. Comparison of the layer group $p6/mmm$ of the intermetallic layer (top row) with the layer group $p2/b11$ of the layer of iodido-bismuthate chains (bottom row). The black outline corresponds to the rectangular base of the unit cell at $z/c = 0$ (intermetallic layer) and $z/c = 1/2$ (iodido-bismuthate layer), respectively.

1.728 deviates by only 0.25% from the $(3)^{1/2}$ ratio of an C -centered orthohexagonal cell and γ is $(90 - 0.064)^\circ$. On the other hand, the iodido-bismuthate layer only shows the symmetry of the oblique layer group $p2/b11$ (Figure 5). When stacked, the alternating layers of two types necessarily induce a lower overall symmetry. Furthermore, mutual adjustment of the layers is achieved through the origin shift of adjacent and next-nearest layers such that their centers of inversion and glide planes do not coincide in the projection perpendicular to the planes. The inclined stacking vector forces the overall symmetry to be only triclinic.

The $\text{Bi}_{14}\text{Rh}_3\text{I}_9$ crystals cleave very easily parallel to the (001) plane, and smooth surfaces can be prepared using a sticky tape. The ED pattern of the $[001]^*$ zone is in accordance with the triclinic unit cell (Figure 6). The HRTEM image of the $[001]^*$ zone shows perfect ordering in the layer plane. It exhibits a predominantly hexagonal pattern with reduced symmetry, created by the inclined stack of intermetallic layers and the overlying iodido-bismuthate chains (Figure 6). The observed atomic ordering fully corresponds to the crystal structure model derived from the X-ray diffraction experiment.

As dictated by the 6-fold symmetry, an intermetallic layer offers multiple equal placements for the adjacent iodido-bismuthate layer including rotations in multiples of 60° along the normal of the intermetallic layer, i.e. c^* . Fortunately, the propagation of the iodido-bismuthate chains can be easily imaged by HRTEM since they contribute prominently to the image contrast in broad ranges of thicknesses and defoci values. Both the X-ray and the TEM investigations confirm that all iodido-bismuthate chains run in parallel along the b axis. This

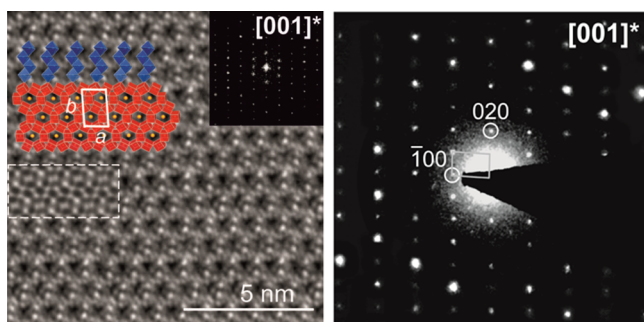


Figure 6. Left: A HRTEM image of the $[001]^*$ zone with an inserted Fourier transform, simulated HRTEM ($d = 8$ nm, $t = 10$ nm), and an overlay with a single intermetallic layer and a single layer of iodido-bismuthate chains. The bright spots correspond to iodine atoms, and gray regions correspond to bismuth and rhodium atoms, while the black spots represent cavities, according to simulations. Right: An experimental diffraction pattern of the $[001]^*$ zone. The unit cell is outlined by a solid white line.

can be seen for example in the HRTEM image of the $[1\bar{1}0]^*$ zone, which also demonstrates a high degree of ordering at the unit-cell level (Figure 7). Parallel orientation of the chains can be associated with the slight deviation of the intermetallic layer from hexagonal metrics. In the underlying case this is apparently sufficient to ensure transmission of the information on chain alignment in the course of crystal growth.

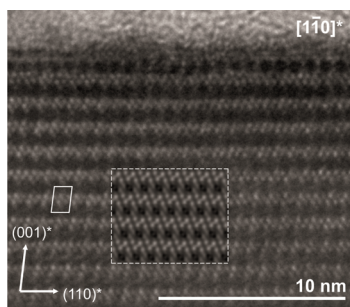


Figure 7. A HRTEM image of the $[1\bar{1}0]^*$ zone with an inserted simulated HRTEM ($d = 20$ nm, $t = 5$ nm). The bright spots correspond to iodine atoms, gray regions correspond to bismuth and rhodium atoms, while the black spots represent cavities, according to simulations. The unit cell is outlined by a solid white line.

The twofold axes, present in the layer groups of both fragments, trigger the formation of polysynthetically twinned crystals. Thereby the inclination of the stacking vector changes in neighboring domains, as has been observed in the X-ray diffraction and the TEM experiments (Figure 8).

Furthermore, deviations from the regular stacking occur if an intermetallic layer is shifted by $b/2$. This can easily happen, since the translation period of the iodido-bismuthate chains is only half of the one of the intermetallic layer. According to the C-centering of the orthohexagonal setting (centering vector $a/2 + b/2$), this shift is equivalent to $a/2$. Such shifts create antiphase boundaries, as seen in the HRTEM images (Figure 8, the unit-cell shift is indicated by an arrow).

With reference to a possible coupling between the topologically nontrivial intermetallic layers, it is noteworthy that at the domain boundaries of both observed defect types the relative position of subsequent intermetallic layers is equivalent to the situation inside the domains.

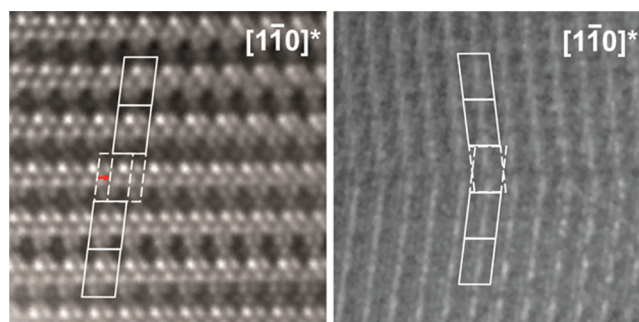


Figure 8. Antiphase domain with a shift (left) and a twin (right) observed in the HRTEM image of the $[1\bar{1}0]^*$ zone. Solid white lines show a row of adjacent unit cells, and dashed lines indicate the hypothetical regular stacking at the domain boundary. The twin boundary appears to lie in an iodido-bismuthate layer. For a twin boundary in the intermetallic layer see Figure S10 of the Supporting Information.

In crystals with a high density of such stacking faults, twin and/or antiphase boundaries, the ordered domains are small and diffuse scattering in the rows of reflections parallel to c^* (Supporting Information Figure S8) jeopardizes the crystal structure determination. This problem was significantly ameliorated with the optimized synthetic protocol, as we were able to produce crystals with less diffuse scattering. Nevertheless, these crystals tend to be twinned and feign a monoclinic cell with $a = 1588$ pm, $b = 914$ pm, $c = 1284$ pm, and $\beta = 102.4^\circ$ ($\alpha \approx \gamma \approx 90.0(4)^\circ$). For the structure solution, the crystal was described as a twin with a mirror plane perpendicular to a being the twin element.

CONCLUSION

The complex physics of topological insulators is now being propelled predominantly on the examples of chemically “simple” compounds, and further structural sophistication is being evaded for the sake of interpretation simplicity, although such systems can amass new physical phenomena.³³ In the present contribution we have demonstrated how these concomitant structural and synthetic challenges can be successfully tackled for the new weak 3D topological insulator $\text{Bi}_{14}\text{Rh}_3\text{I}_9$.

Despite the overall structural complexity of $\text{Bi}_{14}\text{Rh}_3\text{I}_9$, one can single out well-defined structural fragments and narrow the observed real-structure phenomena down to mutual adjustment and interaction of two layer types with different pseudosymmetries. The kagomé-like structural motif based on bismuth cubes is not unique for $\text{Bi}_{14}\text{Rh}_3\text{I}_9$ and is echoed in several compounds, most obviously, in the layered structure of $\text{Bi}_{13}\text{Pt}_3\text{I}_7 = [(\text{Bi}_4\text{Pt})_3\text{I}][\text{Bi}_4\text{I}]_2$,³⁴ where platinum substitutes for rhodium as the centering atom. The differing chemical composition is caused by two types of spacers: the same iodido-bismuthate layers as found in $\text{Bi}_{14}\text{Rh}_3\text{I}_9$ and one-atom-thick layers of iodide ions. Moreover, our preliminary results hint toward yet another member of this structure family in the Bi–Pt–I system.

The optimized synthetic protocol can be straightforwardly used to obtain high-quality single crystals and powders of $\text{Bi}_{14}\text{Rh}_3\text{I}_9$, which can be disseminated for the upcoming physical property measurements. The possibly ruining impact of disorder phenomena, almost inevitable for layered systems, could be minimized thanks to the better insight into the phase

diagram of the ternary system and optimized synthetic conditions.

Generally, the band structure in the very vicinity of the Fermi level can be substantially changed by electronic states induced by stacking faults. On the basis of the knowledge about structure defects, realistic theoretical models of the coupling between the topologically nontrivial layers can be set up. Whether the low-energy stacking faults in $\text{Bi}_{14}\text{Rh}_3\text{I}_9$ crystals have impact on their topological properties should come out from forthcoming theoretical studies.

■ EXPERIMENTAL SECTION

Synthesis and Crystal Growth. After analysis of the $\text{Bi}_{14}\text{Rh}_3\text{I}_9$ stability range, the following synthesis techniques have been established.

Microcrystalline samples of $\text{Bi}_{14}\text{Rh}_3\text{I}_9$ are obtained by high-temperature annealing of a stoichiometric mixture of Bi, Rh, and BiI_3 (molar ratio 11: 3: 3; bismuth, MERCK, treated at 220 °C in H_2 -flow; rhodium, MERCK, > 99.9%; bismuth(III)-iodide, synthesized from the elements and sublimated twice). The starting materials were ground under argon atmosphere in a glovebox. The homogeneous powder was sealed in an evacuated silica ampule. The total mass of the batch was adjusted such that the volume concentration of BiI_3 corresponded to 72 mg/mL. Annealing at 365 °C for at least three days yielded almost phase-pure $\text{Bi}_{14}\text{Rh}_3\text{I}_9$ powders with a small impurity of 2–3% bismuth.

For the growth of larger crystals an ampule with a stoichiometric mixture of Bi, Rh, and BiI_3 (see above) was heated to 700 °C in a tubular furnace at a rate of approximately 600 K/h. Fast cooling to 420 °C (−4 K/min) and then slow cooling to 365 °C (−1 K/h) followed instantaneously. After three days the ampule was quenched in water. This technique reproducibly yields black, platelet-shaped crystals of $\text{Bi}_{14}\text{Rh}_3\text{I}_9$ with sizes up to $1 \times 1 \times 0.2 \text{ mm}^3$. The composition of the crystals according to semiquantitative energy-dispersive X-ray analysis (EDX detector, EDAX, lithium-shifted silicon detector; scanning electron microscope, Carl Zeiss, 982 Gemini; acceleration voltage 20 kV) was Bi 49.1%, Rh 14.2%, I 36.7%. These values agree within the accuracy of the method with the calculated ones: Bi 53.9%, Rh 11.5%, I 34.2%.

Powder X-ray Diffraction (PXRD). Crystals of $\text{Bi}_{14}\text{Rh}_3\text{I}_9$ were characterized by powder X-ray diffraction (PXRD) on a PANalytical X'Pert Pro Powder diffractometer with Debye–Scherrer geometry equipped with a $\text{Ge}(111)$ -monochromator, a rotating sample stage, and a PIXcel detector, using $\text{Cu K}\alpha$ radiation ($\lambda = 154.06 \text{ pm}$). The data were collected in reflection mode using a divergence slit that kept the illuminated sample area constant.

Single-Crystal X-ray Diffraction. Single crystals were measured on a four-circle diffractometer Bruker-Nonius Kappa APEX II CCD, with a Mo tube, a graphite(002) monochromator, and a CCD detector at room temperature. The reflections could be indexed in a triclinic cell with $a = 916.40(2) \text{ pm}$, $b = 1583.68(5) \text{ pm}$, $c = 2556.88(7) \text{ pm}$, $\alpha = 96.154(1)^\circ$, $\beta = 100.162(1)^\circ$, and $\gamma = 90.056(1)^\circ$ which was then used for integration within the APEX software package. Numerical absorption correction was applied using an optimized crystal description. A first structure solution in JANA2006³⁵ revealed a possible smaller triclinic cell with $a = 916.61(3) \text{ pm}$, $b = 1583.61(5) \text{ pm}$, $c = 1429.78(5) \text{ pm}$, $\alpha = 62.746(1)^\circ$, $\beta = 80.922(2)^\circ$, and $\gamma = 89.936(2)^\circ$,³² feigning the above-mentioned larger cell by twinning. The twin is mirrored at the plane perpendicular to a . The whole hkl data set was transformed and written into a $hklf5$ file, and then the structure was refined in SHELXL97³⁶ against F_0^2 .

Thermal Properties. Thermal properties of $\text{Bi}_{14}\text{Rh}_3\text{I}_9$ were analyzed by means of differential scanning calorimetry (DSC) using a Setaram Labsys ATD-DSC device with a k-probe (Ni–Cr/Ni–Al; $T_{\text{max}} = 800 \text{ °C}$) and Al_2O_3 as a reference compound. In addition to these in situ experiments, various samples were tempered for 1 h at predefined temperatures (see Results and Discussion) to analyze ex situ the transitions indicated by the signals in DSC measurements.

Transmission Electron Microscopy. Samples were prepared by grating single crystals over a lacey carbon grid, thus depositing fragments. In addition, thin lamellae were cut from a single crystal perpendicular to the largest facet, i.e., along the stacking direction, with an ultramicrotome (Ultracut, Leica Microsystems) equipped with a diamond knife. Prior to it, the crystal was embedded in the epoxy resin Epon (Fluka) that was then polymerized at 60 °C. The nominal lamella thickness was approximately 50 nm while locally crystalline flakes with a thickness between 5 and 15 nm were observed. High-resolution transmission electron microscopy (HRTEM) and selected area electron diffraction (SAED) studies were performed on a FEI Titan F20 microscope with C_s -correction operating at 80 kV and on a CM20 microscope (Philips) operating at 200 kV. For image acquisition, a $2k \times 2k$ Slow-Scan CCD-Camera (Gatan) was used. Image simulations were done with the JEMS software.³⁷

■ ASSOCIATED CONTENT

Supporting Information

Powder diffraction patterns for analysis of the synthesis and additional electron microscopy data. This material is available free of charge via the Internet at <http://pubs.acs.org>.

■ AUTHOR INFORMATION

Corresponding Author

*E-mail: michael.ruck@tu-dresden.de.

Present Address

^{||}(A.G.) Bruker AXS GmbH, Östliche Rheinbrückenstraße 49, 76187 Karlsruhe, Germany.

Author Contributions

The manuscript was written through contributions of all authors. A.G., M.K., and B.R. performed synthesis and crystal structure determination under supervision of M.R. B.R. conducted and analyzed the DSC and TG experiments. A.I. and W.V.d.B. conducted and interpreted the TEM experiments under the supervision of C.T.K. and U.K. B.R., A.I., and M.R. analyzed stacking disorder as related to TEM. M.R. has supervised the project. All authors have given approval to the final version of the manuscript.

Notes

The authors declare no competing financial interest.

■ ACKNOWLEDGMENTS

This work was supported by the German Research Foundation (DFG) in the framework of the Special Priority Programme (SPP 1666) “Topological Insulators”. We are grateful to Mr. E. Schmid, central facility for electron microscopy, Ulm University, for ultramicrotomy of our samples. We thank Mrs. S. Goldberg and Mrs. E. Kern for SEM/EDX measurements and Mr. A. Wolf (all TU Dresden) for assistance with synthesis. C.T.K. acknowledges the Carl Zeiss Foundation, and W.V.d.B. acknowledges the German Research Foundation (Grant No. KO 2911/7-1).

■ REFERENCES

- (1) Hasan, M. Z.; Kane, C. L. *Rev. Mod. Phys.* **2010**, *82*, 3045.
- (2) Bernevig, A. B.; Hughes, T. L.; Zhang, S.-C. *Science* **2006**, *314*, 1757.
- (3) König, M.; Wiedmann, S.; Brüne, Ch.; Roth, A.; Buhmann, H.; Molenkamp, L.; Qi, X.-L.; Zhang, S.-C. *Science* **2007**, *318*, 766.
- (4) Zhang, H.; Liu, C.-X.; Qi, X.-L. *Nat. Phys.* **2009**, *5*, 438.
- (5) Qi, X.-L.; Hughes, T. L.; Zhang, S.-C. *Phys. Rev. B* **2008**, *78*, 195424.
- (6) Xia, Y.; Qian, D.; Hsieh, D. *Nat. Phys.* **2009**, *5*, 398.

- (7) Hsieh, D.; Qian, D.; Wray, L. *Nature (London, U.K.)* **2008**, *452*, 970.
- (8) Chen, Y. L.; Analytis, J. G.; Chu, J.-H. *Science* **2009**, *325*, 178.
- (9) Hsieh, D.; Xia, Y.; Qian, D. *Phys. Rev. Lett.* **2009**, *103*, 146401.
- (10) Garate, I.; Franz, M. *Phys. Rev. Lett.* **2010**, *104*, 146802.
- (11) Mondal, S.; Sen, D.; Sengupta, K.; Shankar, R. *Phys. Rev. Lett.* **2010**, *104*, 046403.
- (12) Culcer, D. *Phys. E (Amsterdam, Neth.)* **2012**, *44*, 860.
- (13) Kitaev, A. Yu. *Ann. Phys.* **2003**, *303*, 2.
- (14) Vidal, G.; Latorre, J. I.; Rico, E. *Phys. Rev. Lett.* **2003**, *90*, 227902.
- (15) Fu, L.; Kane, C. L. *Phys. Rev. Lett.* **2008**, *100*, 096407; *Phys. Rev. Lett.* **2009**, *102*, 216403.
- (16) Sau, J. D.; Lutchyn, R. M.; Tewari, S. *Phys. Rev. Lett.* **2010**, *104*, 040502.
- (17) Alicea, J. *Rep. Prog. Phys.* **2012**, *75*, 076501.
- (18) Beenakker, C. W. J. *Annu. Rev. Condens. Matter Phys.* **2013**, *4*, 113.
- (19) Kane, C. L.; Mele, E. J. *Phys. Rev. Lett.* **2005**, *95*, 146802–226801.
- (20) Min, H.; Hill, J. E.; Sinitsyn, N. A.; Sahu, B. R.; Kleinmann, L.; MacDonald, A. H. *Phys. Rev. B* **2006**, *74*, 165310.
- (21) Yao, Y.; Ye, F.; Qi, X.-L.; Zhang, S.-C.; Fang, Z. *Phys. Rev. B* **2007**, *75*, 041401(R).
- (22) Ruck, M. *Angew. Chem.* **2001**, *113*, 1222; *Angew. Chem., Int. Ed.* **2001**, *40*, 1182.
- (23) Ruck, M. *Z. Kristallogr.* **2010**, *225*, 167.
- (24) Ruck, M. *Confined Metals and Low Temperature Syntheses*; Scientific Research Report; Max-Planck-Institute for Chemical Physics of Solids: Dresden, 2011.
- (25) Isaeva, A.; Rasche, B.; Ruck, M. *Phys. Status Solidi RRL* **2013**, *1–2*, 39.
- (26) Rasche, B.; Isaeva, A.; Ruck, M.; Borisenko, S.; Zabolotnyy, V.; Büchner, B.; Koepernik, K.; Ortix, C.; Richter, M.; van den Brink, J. *Nat. Mater.* **2013**, *12*, 422.
- (27) Rasche, B.; Ruck, M. Unpublished work, 2013.
- (28) Ruck, M. *Acta Crystallogr., Sect. B* **1996**, *52*, 605.
- (29) The Bi–Rh system: Okamoto, H. *J. Phase Equilib. Diffus.* **2010**, *31*, 204. The Bi–I system: In *Binary Alloy Phase Diagrams*; Massalski, T. B., Ed.; ASM International: Materials Park, OH, 1990; Vol. 1, p 744.
- (30) Ruck, M.; Heich, M. R. *Z. Anorg. Allg. Chem.* **2000**, *626*, 2449.
- (31) Gerisch, A.; Ahrens, E.; Ruck, M. Unpublished work, 2013.
- (32) CSD-425974, Fachinformationszentrum Karlsruhe, D-76344 Eggenstein-Leopoldshafen, Germany (Fax: +49-7247-808-666, E-mail: crysdata@fiz-karlsruhe.de).
- (33) Cava, R. J. *Nat. Mater.* **2013**, *12*, 379.
- (34) Ruck, M. *Z. Anorg. Allg. Chem.* **1997**, *623*, 1535.
- (35) Petricek, V.; Dusek, M.; Palatinus, L. *JANA2006, The Crystallographic Computing System*; Institute of Physics: Praha, Czech Republic: 2011.
- (36) (a) Sheldrick, G. M. *SHELXL97, Programs for crystal structure determination*; University of Göttingen: Göttingen, 1997 (b) Sheldrick, G. M. *Acta Crystallogr., Sect. A* **2008**, *64*, 112.
- (37) Stadelmann, P. *JEMS software*, Version 3.8406U2012, <http://cimewww.epfl.ch/people/stadelmann/jemsWebSite/jems.html>, 2012.